Research Square

Preprints are preliminary reports that have not undergone peer review.
They should not be considered conclusive, used to inform clinical practice,
or referenced by the media as validated information.

Defect–Interface Engineering of Machine Learning-Enhanced Au–VSe2–MXene Nanocomposites with Tuned Electronic States for Trace Antibiotic Sensing

Ezhil Vilian
Dongguk University-Seoul
Sujina Tamang
Inha University
Elangovan Sarathkumar
Sree Chitra Tirunal Institute for Medical Sciences and Technology
Ramapurath S. Jayasree
Sree Chitra Tirunal Institute for Medical Sciences and Technology
Yun Suk Huh
yunsuk.huh@inha.ac.kr
Inha University
Young-Kyu Han
Dongguk University-Seoul

Research Article

Keywords: MXene nanosheets, gold nanoparticles, machine learning, amperometry, furazolidone, electrochemical sensor

Posted Date: April 17th, 2026

DOI: https://doi.org/10.21203/rs.3.rs-9218510/v1

License: This work is licensed under a Creative Commons Attribution 4.0 International License.
Read Full License

Additional Declarations: No competing interests reported.

Version of Record: A version of this preprint was published at Advanced Composites and Hybrid Materials on June 16th, 2026. See the published version at https://doi.org/10.1007/s42114-026-01916-2.

Defect–Interface Engineering of Machine Learning-Enhanced Au–VSe_2–MXene Nanocomposites with Tuned Electronic States for Trace Antibiotic Sensing

Ezhil Vilian[a*], Sujina Tamang[b], Elangovan Sarathkumar[c], Ramapurath S. Jayasree[c], Yun Suk Huh[b*], Young-Kyu Han[a*]

[a]*Department of Energy and Materials Engineering, Dongguk University-Seoul, Seoul 04620, Republic of Korea.*

[b]*Department of Biological Engineering, Inha University, Incheon 22212, Republic of Korea.*

[c]*Division of Biophotonics and Imaging, Biomedical Technology Wing, Sree Chitra Tirunal Institute for Medical Sciences and Technology, Poojappura, Thiruvananthapuram, 695012, Kerala, India*

Corresponding authors[*]:

*Department of Energy and Materials Engineering, Dongguk University-Seoul, Seoul 04620, Republic of Korea. E-mail: ezhil2040@dongguk.edu (*E.Vilian*)*

Department of Biological Engineering, Inha University, Incheon 22212, Republic of Korea. E-mail: yunsuk.huh@inha.ac.kr (Y.S. Huh)

Department of Energy and Materials Engineering, Dongguk University-Seoul, Seoul 04620, Republic of Korea. E-mail: ykenergy@dongguk.edu (Y.-K. Han)

Abstract

Ensuring food safety requires engineered hybrid composites with hierarchical interfacial architectures capable of detecting trace antibiotics in complex food and environmental matrices. Here, we report an electrochemical sensing platform based on gold nanoparticle (AuNP)-decorated VSe_2-MXene hybrid nanocomposite for on-site detection of furazolidone (FZD). The VSe_2-MXene scaffold, synthesized via a one-step hydrothermal method, enables in situ anchoring and near-atomic-scale AuNP deposition through chemical reduction. This structural integration induces lattice compression, generating abundant active sites and enhanced electron mobility that facilitate efficient interfacial charge transfer. Comprehensive physicochemical analyzes show that hydrothermal synthesis followed by chemical reduction enables uniform AuNP anchoring on the VSe_2-MXene framework while converting surface M–OH groups into M–O bonds. This interfacial electronic modulation enhances electron-transfer kinetics and selective FZD adsorption. The resulting Au-VSe_2-MXene sensor exhibits significantly reduced charge-transfer resistance (~45 Ω) and an enhanced heterogeneous electron-transfer rate (1.68×10^{-2} cm s^{-1}), enabling a low cathodic peak potential of -0.40 V (vs. Ag/AgCl). The sensor demonstrates a wide linear detection range (6-255 nM, $R^2 = 0.9383$), an ultralow detection limit (0.21 nM), high sensitivity (0.597 μA nM^{-1} cm^{-2}), and excellent long-term stability (>30 days), enabling reliable trace-level FZD detection in real samples even in the presence of common interferents. Machine learning-driven analysis of amperometric i-t currents enabled precise FZD quantification, reducing calibration errors; the Random Forest model (R^2 = 0.997) integrated with IoT supports real-time monitoring for diagnostic and environmental applications.

Keywords: MXene nanosheets; gold nanoparticles; machine learning; amperometry; furazolidone; electrochemical sensor.

1 Introduction

Global water scarcity is worsened by pollution from industrial, agricultural, and wastewater sources. In particular, extensive antibiotic use causes persistent residues in water systems, posing risks to ecosystems and human health [1, 2]. Among these, the nitrofuran antibiotic furazolidone (FZD) has attracted particular attention due to its extensive application in controlling infections caused by pathogens such as *Staphylococcus, Escherichia coli, Shigella*, and *Salmonella* in livestock and aquaculture [3, 4]. FZD residues can enter the environment through contaminated wastewater, manure, biosolids, and agricultural runoff, leading to accumulation in soil, water, and food matrices [5]. These residues pose serious toxicological risks, including systemic toxicity, hematopoietic suppression, and genotoxic effects such as mutagenesis and carcinogenesis [6]. Long-term exposure studies have also linked chronic FZD intake with increased tumor incidence. Therefore, regulatory agencies have established strict safety limits, with permissible levels as low as 1.0 μg kg^{-1} [7, 8]. The increasing demand for intelligent environmental and biomedical monitoring makes trace-level detection of FZD in complex matrices challenging, requiring highly sensitive analytical methods and advanced electrode materials for reliable analysis [9].

Several conventional analytical techniques and emerging sensing platforms have been explored for in situ detection of FZD, including high-performance liquid chromatography (HPLC), electrochemical methods, liquid chromatography-tandem mass spectrometry (LC-MS/MS),

fluorescence and chemiluminescence assays, and enzyme-linked immunosorbent assay (ELISA) [10, 11]. Although these techniques provide reliable analytical performance, their practical application is often limited by complex procedures, expensive instruments, and the need for skilled operators. In contrast, electrochemical (EC) sensors provide a promising alternative because of their simple operation, low cost, portability, and minimal sample requirements, enabling rapid analysis of real samples [12]. However, EC detection of FZD in plant matrices remains difficult due to its very low environmental concentration and the complex composition of plant tissues. Many reported studies rely on artificially spiked samples that may not reflect real environmental conditions. Therefore, there is a need to develop highly sensitive and selective electrode materials through rational nanomaterial engineering for reliable trace-level detection of FZD in complex matrices [13].

The development of tailor-engineered electroanalytical sensors provides considerable strengths; however, the intricacy of their output signatures can lead to misinterpretation, creating a substantial challenge for non-specialist users [14, 15]. Machine learning (ML) architectures can effectively interpret complex electrochemical signal patterns frequently unrecognized by conventional analytical methods, thereby improving analyte detection, classification, and quantification [16]. The combination of Internet of Things (IoT) connectivity enhances convenience through the provision of intuitive, real-time, and user-friendly data interfaces. The integration of state-of-the-art sensing platforms with computational analytics enhances decision-making and expediates more effective strategies for managing water pollution [17].

Modern materials design increasingly focuses on advanced component selection, including oxides, metals, alloys, conductive polymers, and carbides, combined with tailored microstructures such as porous frameworks, core-shell architectures, and hierarchical nanostructures [18]. In addition, precision hybridization strategies such as doping, decorating, and encapsulation are widely employed to tune material properties. Within this context, defect engineering and interfacial architecture design have become important strategies for developing next-generation functional materials [19]. These approaches allow controlled composition, generation of vacancy-rich heterointerfaces, and strong defect-interface synergy, which can significantly enhance electron mobility and catalytic performance [20]. Transition metal dichalcogenides (TMDs), such as VS_2, MoS_2, WS_2, ReS_2, CoS_2, and TiS_2, have been widely investigated for electrochemical applications. Among them, VSe_2 is particularly attractive due to its layered metallic structure, high electrical conductivity, and chemical stability [21, 22]. Its graphene-like layers are connected by weak van der Waals interactions, providing large surface area and tunable electronic properties [23]. However, the intrinsic conductivity attenuation, limited active edge sites, and structural instability of VSe_2 can restrict catalytic efficiency and selectivity in electrochemical systems [24].

To overcome these limitations, noble metal nanostructures such as Ag, Au, Ru, and Pd have been incorporated into VSe_2-based architectures to enhance conductivity, catalytic activity, and signal amplification [25, 26]. Among these materials, gold nanoparticles (AuNPs) are especially suitable for sensing applications because of their excellent chemical stability and strong catalytic activity [27]. Their filled d^{10} electronic configuration facilitates analyte adsorption and accelerates interfacial electron transfer [28]. However, the high cost and limited availability of noble metals

encourage the development of hybrid systems with low noble-metal loading. Integrating AuNPs with two-dimensional materials offers a cost-effective strategy while maintaining high catalytic performance [29]. The incorporation of AuNPs with VSe_2 enhances structural stability and adsorption capacity, improving electrochemical sensing capability. Many existing sensor platforms still depend on extensive fabrication processes or operate optimally only under alkaline environments [30]. Hybrid architecture integrating the inherent conductivity of 2D materials with the signal-amplification capabilities of AuNPs offers a viable way to achieving high sensitivity in environmentally and physiologically relevant settings [31].

MXenes, a family of two-dimensional transition metal carbides and nitrides such as Ti_3C_2, Ti_2C, Nb_2C, and V_2C, have attracted significant interest for environmental sensing because of their layered structure, large surface area, metallic conductivity, and diverse surface terminations [32]. Nevertheless, pristine MXenes often suffer from high surface free energy, oxidation susceptibility, and structural instability [33]. These challenges can be mitigated through defect engineering and interface design, which generate vacancy-rich heterointerfaces and tailored surface chemistries that enhance conductivity and catalytic activity. In particular, V_2C MXene with –O, –OH, and –F surface groups provides suitable nucleation sites for anchoring metal nanoparticles and controlling crystal growth [34]. Based on these considerations, hybrid architectures combining VSe_2, MXene, and Au nanoparticles provide an effective strategy for constructing advanced electrocatalysts Such systems can suppress layer restacking, improve structural stability, and increase active-site density [35]. Therefore, we hypothesized that incorporating AuNPs into a VSe_2-MXene matrix would accelerate interfacial electron transfer and significantly improve electrocatalytic sensing

performance

In this work, we synthesized an Au-VSe_2-MXene hybrid nanostructure through a one-step hydrothermal process followed by chemical reduction for AuNP deposition. The resulting composite exhibits hierarchical morphology and well-defined interfacial architecture with uniformly dispersed AuNPs. This structural integration enhances electron-transfer kinetics and catalytic activity for FZD detection. The Au-VSe_2-MXene sensor showed low charge-transfer resistance (~45 Ω) and a high heterogeneous electron-transfer rate constant (1.68×10^{-2} cm s^{-1}). The sensor demonstrated a wide linear detection range (6-255 nM), an ultralow detection limit (0.24 nM), and high sensitivity. In addition, it exhibited excellent reproducibility and stability with more than 90% signal retention after 30 days. Furthermore, amperometric current signals were analyzed using optimized tree-based machine learning model (Random Forest) and subsequently integrated with IoT platforms for real time connectivity. This approach enabled accurate FZD classification and real-time remote monitoring, demonstrating the potential of the developed nanomaterial platform for environmental monitoring and diagnostic applications.

2 Experimental Section

2.1 Materials and Reagents

Hydrofluoric acid (≥48%), furazolidone (FZD, ≥99%), vanadium(III) acetylacetonate, selenium dioxide (SeO_2), Na_2HPO_4 (≥99.99%), hydrogen tetrachloroaurate(III) ($HAuCl_4$, ≥99%), Nafion® 5% solution, NaH_2PO_4 (≥98%), NaOH (≥99.99%), L-ascorbic acid (≥99%), and H_2SO_4 (≥99.999%) were purchased from Sigma-Aldrich. Vanadium aluminum carbide (V_2AlC, MAX phase; <40 μm, ≥95% purity) was

obtained from Carbon-Ukraine Ltd. PBS (0.05 M, pH 7.0) was prepared from NaH_2PO_4/Na_2HPO_4, and electrolyte pH (3-9) was adjusted using 0.1 M H_2SO_4 or NaOH. A 10 mM FZD stock solution was freshly prepared daily in PBS and diluted to 10^{-1}-10^{-3} M for standards. All solutions were prepared with ultrapure water (18.2 MΩ·cm, Milli-Q) and without further purification.

2.2 Structural Characterization

FTIR spectra were collected on a JASCO FT/IR-6600 (4000-400 cm^{-1}), and UV-Vis spectra of FZD were recorded on a JASCO V-770 (200-800 nm, 1 cm quartz cuvettes). Au content was quantified by ICP-OES (Thermo Fisher Scientific). Electrochemical studies, including CV, LSV, and amperometric i-t measurements, were conducted at 25 °C using a CHI 7045E potentiostat in a three-electrode setup, with Au-VSe_2-MXene-modified SPCE as the working electrode, a platinum wire counter, and Ag/AgCl (saturated KCl) reference. EIS was performed in 0.1 M KCl containing 5 mM $[Fe(CN)_6]^{3-/4-}$ with a 5 mV AC perturbation over 0.1 Hz-100 kHz. All measurements were conducted in N_2-deaerated 0.05 M PBS (pH 7.0). Micro and nanostructures were examined via HRSEM (Hitachi SU8010) and HRTEM (JEOL JEM-2100F), with elemental mapping by EDX. Powder X-ray diffraction (XRD) patterns were recorded on a PANalytical X'Pert Pro diffractometer using Cu Kα radiation (λ = 0.1541 nm). X-ray photoelectron spectroscopy (XPS) was performed on a Thermo Fisher K-Alpha instrument, with spectra deconvoluted using XPS Peak 41 and referenced to the C 1s peak at 284.6 eV.

The standard heterogeneous electron-transfer rate constant (k°) of each modified electrode was determined by equivalent circuit fitting using Eq. (1)[36].

$$k^0 = \frac{RT}{n^2F^2R_{ct}AC} \qquad (1)$$

where R is the universal gas constant (8.314 J mol^{-1} K^{-1}), T is the temperature (298 K), n is the number of electrons transferred (n=1 for 5 mM $[Fe(CN)_6]^{3-/4-}$, F is the Faraday constant (96,485 C mol^{-1}), A is the electrode surface area, and C is the concentration of the redox species (0.005 M). The electron-transfer coefficient (α) and heterogeneous rate constant (k_s) were subsequently calculated using the Laviron and Velasco equations (2) and (3), respectively [37, 38]:

$$E_{pc} = \mathrm{E^o} + \left(\frac{RT}{\alpha nF}\right)\ln\left(\frac{RTks}{\alpha nF}\right) + \left(\frac{RT}{\alpha nF}\right)\ln\nu \qquad (2)$$

$$k_s = 2.415\exp\left(\frac{-0.02F}{RT}\right)D^{1/2}(E_P - E_{p/2})^{-1/2}\nu^{1/2} \qquad (3)$$

where n is the number of electrons transferred, ν is the scan rate, α is the electron-transfer coefficient, E^o is the standard potential, E_p is the peak potential, and $E_{p/2}$ is the potential corresponding to half the peak current. According to the Nernst equation ($E_{pc} = E^0$ - [(2.303 mRT)/nF] × pH). Based on the calibration plot, the sensor's analytical performance was assessed by calculating the limit of detection (LOD) and limit of quantification (LOQ), determined using the standard expressions: LOD = 3.3σ/S and LOQ = 10σ/S, where σ is the standard deviation of the blank signal (0.003 μA, averaged over five independent measurements) and S is the slope of the calibration curve.

2.3 Synthesis of Ultrathin MXene

Ultrathin V_2C MXene sheets were obtained by selectively etching Al from V_2AlC MAX phase. Briefly, 1 g V_2AlC was gradually added to 20 mL concentrated HF under stirring (400 rpm) and reacted at 35 °C

for 48 h. The suspension was repeatedly centrifuged (7000 rpm, 15 min), washed to neutral pH, vacuum-filtered through a 0.2 μm PTFE membrane, and freeze-dried at -40 °C for 48 h. The delaminated MXene was stored under vacuum (<10 Torr) at 25 °C and used within 24 h to minimize oxidation.

2.4 Synthesis of VSe_2-MXene Nanocomposite

VSe_2-MXene nanocomposites were synthesized hydrothermally by dispersing vanadium(III) acetylacetonate (1 mmol), SeO_2 (4 mmol), and V_2C MXene (120 mg) in 30 mL ultrapure water, followed by incremental addition of oxalic acid (19.5 mmol) and choline chloride (10 mmol) and sonication (37 kHz, 150 W, 30 min). The mixture was transferred to a 100 mL Teflon-lined autoclave and heated at 200 °C for 24 h (ramp rate 5 °C min^{-1}). The black precipitate was vacuum-filtered, washed with ethanol and water, dried, and annealed under N_2 at 300 °C for 3 h (ramp rate 2 °C min^{-1}). Pristine VSe_2 was prepared under identical conditions without MXene.

2.5 Preparation of Au-Decorated VSe_2-MXene Nanocomposites

Au-VSe_2-MXene composites were prepared by dispersing 1 g VSe_2-MXene in 100 mL 1:1 water/ethanol, adding $HAuCl_4 \cdot 3H_2O$ (5 mg/mL, 100-600 μL) at desired Au ratios, stirring 30 min, and sonication for 1 h at 25 °C. Reduction was achieved by dropwise addition of 50 μL 0.01 M ascorbic acid, followed by 30 min stirring. The product was collected by centrifugation (6000 rpm, 5 min), washed with ethanol and water, and vacuum-dried at 40 °C for 24 h. Control materials (Au-MXene, Au-VSe_2) were synthesized similarly.

2.6 Fabrication of Au-VSe_2-MXene-Modified Electrodes

For SPCE fabrication, commercial SPCEs (3 mm diameter, 0.0706 cm^2) were activated via CV in 1:3 H_2SO_4/H_2O_2 for three cycles (-1.0 to +1.0 V, 10 mV s^{-1}), rinsed with ethanol and water, dried under vacuum at 25 °C, and stored in a desiccator. Catalyst ink was prepared by dispersing 1 mg Au-VSe_2-MXene in 480 µL water, 480 µL ethanol, and 40 µL Nafion 117, ultrasonicated 30 min, and 3 µL was drop-cast onto SPCEs, dried under infrared light for 20 min, and rinsed to remove loose particles. For flexible electrodes, Au-VSe_2-MXene was deposited on laser-induced graphene (LIG) fabricated via mask-free CO_2 laser patterning of 250 µm polyimide at 8% engraving speed and 10% power, yielding a three-electrode configuration (1.1 mm working, reference, counter). Surface residues were removed with N_2, wiring insulated with PI tape, contact pads affixed with copper tape and silver paste, and the reference electrode completed by applying Ag/AgCl ink and curing at 80 °C for 15 min. SPCEs modified with MXene, VSe_2, VSe_2-MXene, Au-VSe_2, Au-MXene, and Au-VSe_2-MXene were prepared following the same protocol. A schematic of the fabrication process is shown in Figure 1a.

2.7 Machine Learning

Machine learning based regression analysis was performed using scikit-learn to correlate electrochemical response with analyte concentration. The dataset comprised 19 concentration levels with five replicates each (95 samples). Three input features mean current, its logarithmic transformation, and signal slope were used, with concentration as the target. All features were standardized using z-score normalization to ensure uniform scaling. Principal Component Analysis (PCA) was applied to evaluate data variability and feature contributions. The dataset was split into training and testing sets (80:20). Four regression models Linear Regression, Random Forest, K-Nearest Neighbors (KNN), and Multi-layer Perceptron

(MLP) were implemented to capture linear and nonlinear relationships. Hyperparameters for nonlinear models were optimized using grid search with 5-fold cross-validation. Model performance was assessed using R^2, RMSE, and MAE. Additional validation included cross-validation stability, predicted vs. actual plots, residual analysis, and learning curves to ensure robust generalization without overfitting.

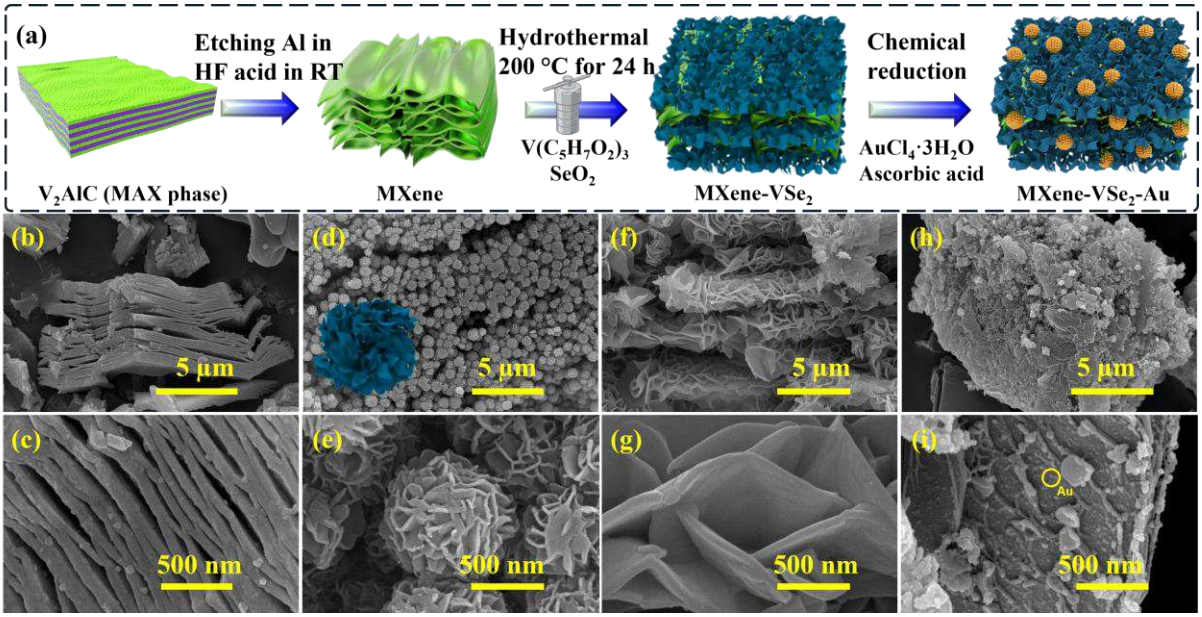

Figure 1: (a) Schematic of the Au-VSe_2-MXene-SPCEs fabrication. SEM images of (b-c) MXene, (d-e) VSe_2, (f-g) VSe_2-MXene, and (h-i) Au-VSe_2-MXene.

3 Results and Discussion

3.1 Fabrication and Morphological and Elemental Analysis of Au-VSe_2-MXene composites

The catalyst synthesis is outlined in Figure 1a. Briefly, Au-VSe_2-MXene was prepared through a three-

step procedure. First, concentrated HF selectively etched the V_2AlC MAX phase at room temperature, removing Al layers and producing accordion-like V_2C MXene. VSe_2 was then grown in situ on the MXene via a hydrothermal process, during which oxalic acid and choline chloride promoted nucleation on the MXene surface. Finally, Au nanoparticles were deposited onto the VSe_2-MXene by chemical reduction of $HAuCl_4 \cdot 3H_2O$, yielding uniformly assembled Au^0 across the nanoflake structure. Control samples of Au-MXene and Au-VSe_2 were also synthesized for comparison.

The morphology, structural characteristics, and surface chemistry of the Au-VSe_2-MXene hybrid were systematically analyzed using electron microscopy, XPS, XRD, and FTIR spectroscopy. MXene displayed the characteristic multilayered, accordion-like architecture produced during selective etching of the V_2AlC precursor (Figure 1b-c). The VSe_2 had wrinkled and crumpled nanosheets forming hierarchical nanoflower-like superstructures (Figure 1d-e), promoting electrochemical activity due to many edge and defect sites. After integrating VSe_2 with MXene nanoflowers were evenly dispersed across the surface without particle aggregation (Figure 1f-g), indicating strong compatibility between the layered VSe_2 and MXene frameworks. A ternary Au-VSe_2-MXene material with uniformly anchored Au NPs decorated with the defect-rich hybrid scaffold (Figure 1h-i). HRTEM verified the hierarchical arrangement of VSe_2 and the integrity of the multilamellar structure of MXene (Figure 2a-d). VSe_2 nanosheets are evenly distributed in MXene layers in the VSe_2-MXene composite (Figure 2e-f), indicating successful hybrid formation. The HRTEM images of the Au-VSe_2-MXene composite (Figure 2g-h) demonstrated an even distribution of Au NP at the VSe_2-MXene interface. Selected-area electron diffraction (SAED) patterns exhibited well-defined diffraction rings indexed to the (111), (200), (220), and (311) crystallographic planes of face-centered cubic (fcc) Au, unequivocally confirming the

formation of metallic Au NPs. Lattice-resolved TEM analysis demonstrated interplanar distances of 0.60 nm, attributable to the (001) crystallographic plane of hexagonal VSe_2, and 0.24 nm, corresponding to the (111) plane of fcc Au. EDS elemental mapping revealed a consistent spatial distribution of Au, V, Se, and N throughout the composite (Figure 2i). Quantitative EDX and ICP-OES measurements were consistent, revealing an Au loading of approximately 5 wt% (Figure 2j).

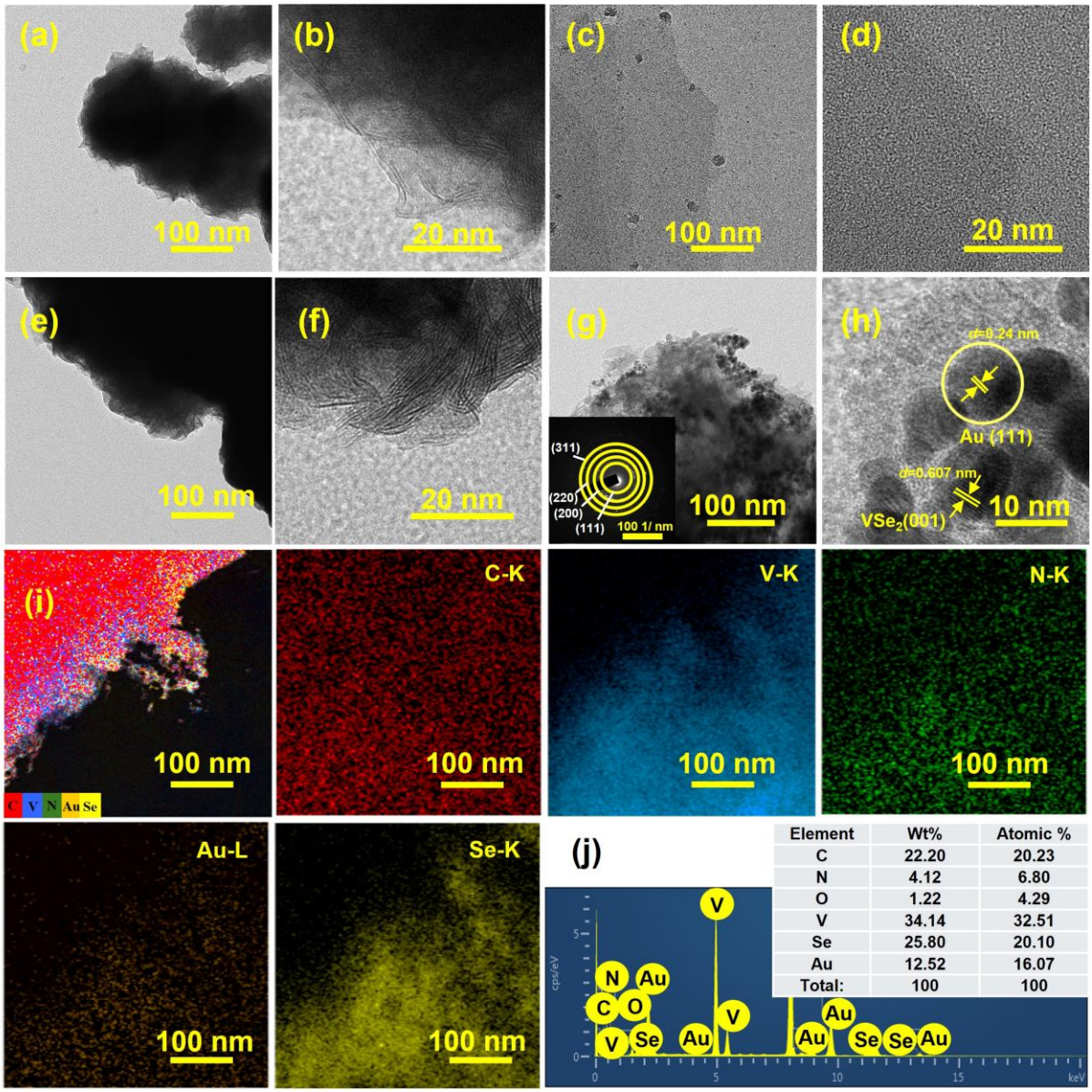

Figure 2: HRTEM images of (a-b) VSe_2, (c-d) MXene, (e-f) VSe_2-MXene, and (g-h) Au-VSe_2-MXene; inset in (g) shows SAED pattern. (i) Elemental mapping and (j) EDX spectrum of the Au-VSe_2-MXene composite.

XPS was used to examine the synthesized Au-VSe_2-MXene surface chemical composition and valence states. The survey spectrum (Figure 3a) of the Au-VSe_2-MXene architecture shows C 1s, N 1s, Au 4f, Se 3d, and V 2p with binding energies of 284, 400, 84, 54, and 515 eV, matching EDS elemental distribution. The high-resolution C 1s spectra shows five peaks at 283.6, 284.6, 285.5, 286.8, and 288.3 eV (Figure 3b) for MXene's V–C, sp^2 C–C, C–N, C=O, and O–C=O surface terminations typical of MXene. The V 2p spectrum shows multiple spin–orbit doublets, with V^{4+} peaks at 517.2 and 524.4 eV, small V^{3+} peaks at 515.4 and 523.2 eV, and V^{2+} peaks at 513.7 and 521.3 eV (Figure 3c), confirming mixed-valence states in MXene composites with surface terminations and defect-rich structures. Deconvolution of the N 1s spectrum revealed characteristic peaks centered at 398.6, 400.2, 401.3, and 402.9 eV, corresponding to pyridinic, pyrrolic, graphitic, and oxidized nitrogen functionalities, respectively (Figure 3d), originating from choline chloride. The amine nitrogen functions as a donor site capable of forming coordination bonds with metal centers. Pyridinic and pyrrolic nitrogen species provide catalytically active sites that can interact with protons and adsorbed FZD molecules, whereas graphitic nitrogen enhances the electrical conductivity of the VSe_2-MXene framework, thereby facilitating charge-transfer kinetics during FZD sensing. The Se 3d spectrum exhibits a doublet at 54.2 and 54.9 eV (Figure 3e), attributed to Se^{2-} ($3d_{5/2}$ and $3d_{3/2}$) in hexagonal VSe_2. Deconvolution of the O 1s core-level spectrum yielded three distinct peaks at 532.0, 531.3, and 530.5 eV, corresponding to surface-adsorbed V–C–$(OH)_x$, V–C–O_x, and lattice V–O functionalities, respectively. In the Au 4f spectrum (Figure 3g), the peaks at 84.1 and 87.8 eV with a 3.7 eV spin–orbit separation correspond to metallic Au^0, and their slight positive shift indicates interfacial charge transfer to the selenium-deficient VSe_2-MXene surface. Treatment with dilute $HAuCl_4 \cdot 3H_2O$ oxidized and etched the metallic Au, producing Au NP that strongly interact with the

VSe_2-MXene framework, induce electron redistribution, and achieve uniform Au dispersion, thereby optimizing dual active sites for enhanced electrocatalytic sensing activity.

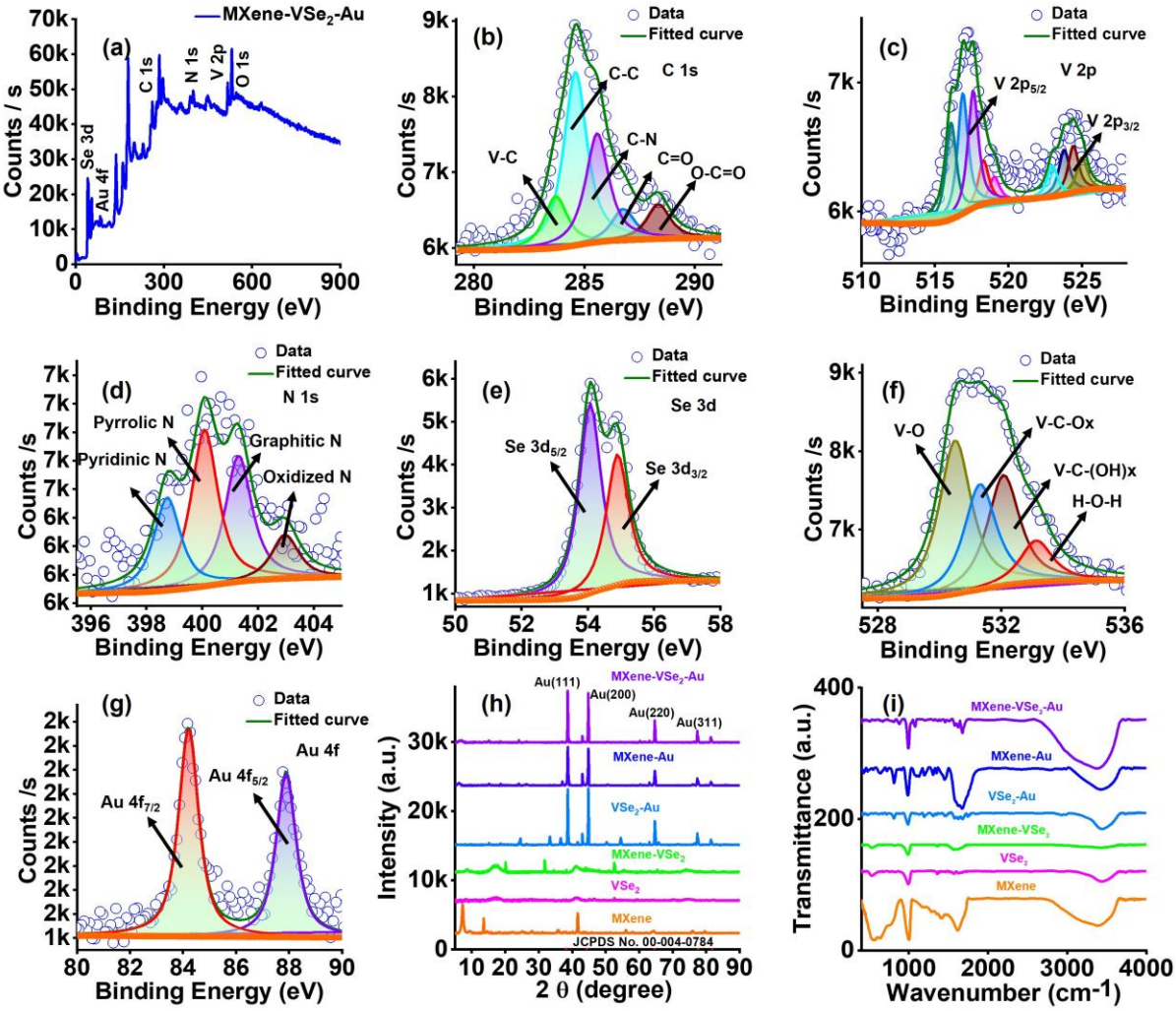

Figure 3: (a) Full XPS survey of Au-VSe_2-MXene; high-resolution spectra of (b) C 1s, (c) V 2p, (d) N 1s, (e) Se 3d, (f) O 1s, and (g) Au 4f. (h) XRD pattern and (i) FTIR spectrum.

The crystalline phases of the synthesized Au-VSe_2-MXene architecture were examined using X-ray diffraction (XRD) analysis (Figure 3h). The diffraction pattern of MXene displayed reflections at 7.6°, 13.6°, 25.1°, 35.8°, 41.6°, corresponding to the (002), (004), (006), (100), and (103), (104), planes, respectively for V_2C MXene. The VSe_2 pattern showed characteristic peaks at 2θ of 17.1, 28.1, 41.45, 46.7, indexed to (001), (002), (102), and (003) plane of hexagonal-phase VSe_2 nanosheets (JCPDS 01–089-1641). Compared with pristine VSe_2, the VSe_2-MXene composite exhibited noticeably broadened peaks for these reflections, indicating reduced crystallite size and the formation of VSe_2 nanocrystallites due to interfacial coupling. Diffuse diffraction peaks centered at 38.6°, 44.9°, 64.7°, and 77.1° were detected in the Au-VSe_2 pattern, indexed to the (111), (200), (220), and (311) reflections of face-centered cubic Au (JCPDS 04-0784), indicating the presence of surface-associated metallic Au^0. The Au-MXene retained both the intrinsic MXene reflections along with the characteristic Au peaks. These Au reflections were also clearly observed in the Au-VSe_2-MXene composite, confirming successful anchoring and surface passivation of Au NP onto the VSe_2-MXene framework.

FTIR spectroscopy was used to analyze the structural information and interaction between Au NP active phase and VSe_2-MXene architecture from 400 to 4000 cm^{-1} (Figure 3i). The MXene spectrum exhibited characteristic absorption bands vibrational modes for O–H, C=O, C–O, C-O-C and V–C, at 3428, 1660, 1414, 1000, and 568 cm^{-1}, respectively. VSe_2 showed typical bands for V-Se, V-O, and -OH at 525, 962-1714, and 3431 cm^{-1}, respectively. The VSe_2-MXene composite effectively integrated VSe_2 into the MXene nanosheet structure, as evidenced by absorptions at 670 and 578 cm^{-1}. The Au-MXene composite displayed additional absorption bands at 505 and 793 cm^{-1}, attributed to C=O and V–O stretching vibrations, respectively, indicating the successful incorporation of Au onto the MXene surface. The Au-

VSe_2 sample showed a pronounced reduction in –OH and V–Se band intensities, indicating Au-induced surface modification. The FTIR spectrum of Au-VSe_2-MXene closely matched those of Au-VSe_2 and Au-MXene, confirming Au incorporation into the VSe_2-MXene heterostructure.

3.2 Electrocatalytic performance of sensing electrodes

The interfacial electron-transfer characteristics of various sensing electrodes were probed using EIS technique (Figure 4a). Experiments were conducted in 0.1 M KCl containing 5 mM $[Fe(CN)_6]^{3-/4-}$, applying a 5 mV AC perturbation over a frequency range of 0.1 Hz to 100 kHz. The resulting Nyquist plots were analyzed using a conventional Randles equivalent circuit comprising the solution resistance (R_s), charge-transfer resistance (R_{ct}), a constant-phase element (CPE) representing double-layer capacitance, and the Warburg diffusion element (Z_w). The bare electrode exhibited a pronounced semicircle with an R_{ct} of 218 Ω, indicating sluggish electron-transfer kinetics. Incorporation of VSe_2 increased R_{ct} to 332 Ω. Due to their semiconducting nature and negatively charged surface of VSe_2 nanosheets, which hinder the anionic redox probe. Modification with MXene reduced R_{ct} to 159 Ω, while the VSe_2-MXene hybrid further decreased it to 108 Ω, demonstrating improved conductivity due to synergistic interactions between the VSe_2 and MXene. The R_{ct} values of 80 Ω and 60 Ω for Au-VSe_2 and Au-MXene indicate excellent metallic conductivity of Au. The ternary Au-VSe_2-MXene sensor had the lowest R_{ct} (45 Ω), indicating the most effective electron-transfer channel due to the combined electroactive and synergistic contributions of Au and VSe_2-MXene architecture.

Equivalent circuit fitting was employed to determine the standard heterogeneous electron-transfer rate constant (k°) for each electrode using Eq. (1), with increasing values as follows: VSe_2 (3.39×10^{-3} cm s^{-}

^{1}) < bare electrode (2.23 x 10^{-3} cm s^{-1}) < MXene (4.65 x 10^{-3} cm s^{-1}) < VSe_2-MXene (6.85 x 10^{-3} cm s^{-1}) < Au-VSe_2 (9.44 x 10^{-3} cm s^{-1}) < Au-MXene (1.26 x 10^{-2} cm s^{-1}) < Au-VSe_2-MXene sensor (1.68 x 10^{-2} cm s^{-1}). Catalytic activity was further assessed via CV in 5 mM $[Fe(CN)_6]^{3-/4-}$ and 0.1 M KCl at 50 mV s^{-1} (Figure 4b). The peak-to-peak separation ($\Delta Ep = E_{pa}-E_{pc}$) and I_{pa}/I_{pc} ratios for VSe_2, bare electrode, MXene, VSe_2-MXene, Au-VSe_2, and Au-MXene were 388, 262, 250, 205, 178, 169 mV and 3.72, 3.52, 2.71, 2.19, 1.94, 1.88, respectively. The Au-VSe_2-MXene sensor exhibited the lowest ΔEp (150 mV) and I_{pa}/I_{pc} ratio (1.74) with well-defined redox peaks, indicating markedly enhanced electron-transfer kinetics for rapid on-site FZD sensing.

The electrocatalytic sensing performance of bare and various sensing electrodes toward FZD was evaluated using CV method in N_2-saturated 0.05 M PBS (pH 7), scanning from +0.2 to -0.8 V at 50 mV s^{-1}, in the presence and absence of FZD (Figure 4c-d). In the absence of 500 µM FZD, the Au-VSe_2-MXene exhibited a higher background current than bare, VSe_2, MXene, VSe_2-MXene, Au-VSe_2, and Au-MXene, attributed to interfacial engineering and the synergistic interaction between Au and the VSe_2-MXene framework (Figure SI 1). Upon introducing 500 µM FZD, bare and VSe_2 showed broad, poorly defined cathodic peaks at -0.56 V and -0.63 V with currents of 5.94 and 5.77 µA, respectively, reflecting sluggish electron-transfer kinetics, semiconductor behavior, and weak FZD adsorption. MXene delivered a broader cathodic response at -0.47 V (10.47 µA), indicating limited electrocatalytic activity due to MXene instability despite its high surface area and functional groups (–F, –O, –OH). The VSe_2-MXene exhibited improved activity, with a cathodic overpotential of -0.45 V and a current of 10.92 µA. Incorporation of Au in Au-VSe_2 and Au-MXene shifted the cathodic onset to -0.43 and -0.42 V with currents of 12.35 and 15.52 µA, respectively, highlighting Au NPs role in enhancing direct electron

transfer, though surface fouling from FZD byproducts persisted. Optimization of Au loading (100-600 μL) revealed a peak current at 400 μL, with excessive loading causing aggregation and diffusion limitations (Figure SI 2). The Au-VSe_2-MXene showed the highest performance, producing a distinct irreversible cathodic peak at -0.40 V with a current of 25.76 μA. The defect-rich VSe_2-MXene framework provides abundant active sites, facilitates analyte diffusion, and effectively anchors Au, resulting in strong synergistic electrocatalytic behavior. These results confirm a two-step $2e^-/2H^+$ reduction of FZD on Au-VSe_2-MXene sensor: the nitro group is first reduced to a nitroso (–N=O) intermediate, followed by conversion to a hydroxylamine (–NHOH) derivative (Scheme 1).

3.3 Experimental parameter optimization

To investigate the electron-transfer kinetics of FZD, CVs were recorded at scan rates from 10 to 1000 mV s^{-1} using Au-VSe_2-MXene sensor in 0.05 M PBS containing 200 μM FZD (Figure 4e-f). The cathodic peak current (I_{pc}) increased linearly with the square root of the scan rate ($\nu^{1/2}$), accompanied by a positive shift in cathodic peak potential (E_{pc}), confirming the irreversibility of FZD reduction. This potential shift arises from diffusion-layer variations: at low scan rates, a thicker diffusion layer limits species flux, requiring greater overpotential and producing a more negative E_{pc}, whereas at high scan rates, a thinner layer enhances the concentration gradient, shifting E_{pc} positively. The linear I_{pc}-$\nu^{1/2}$ relationship indicates diffusion-controlled kinetics. E_{pc} also varied linearly with ln ν, described by E_{pc} (V) = -0.0205 ln ν + 0.4733 ($R^2 = 0.9901$). Electron-transfer parameters, including the transfer coefficient ($\alpha = 0.63$) and heterogeneous rate constant ($k_s = 1.0 \times 10^{-2}$ cm s^{-1}), were determined using the Laviron and Velasco equations (2) and (3). The process involves n = 2 electrons per step, consistent with a two-step

nitro group reduction: first to a nitroso intermediate, then to hydroxylamine, each step involving a coupled $2e^-/2H^+$ transfer, confirming the mechanistic pathway of FZD electroreduction at the Au-VSe_2-MXene sensor.

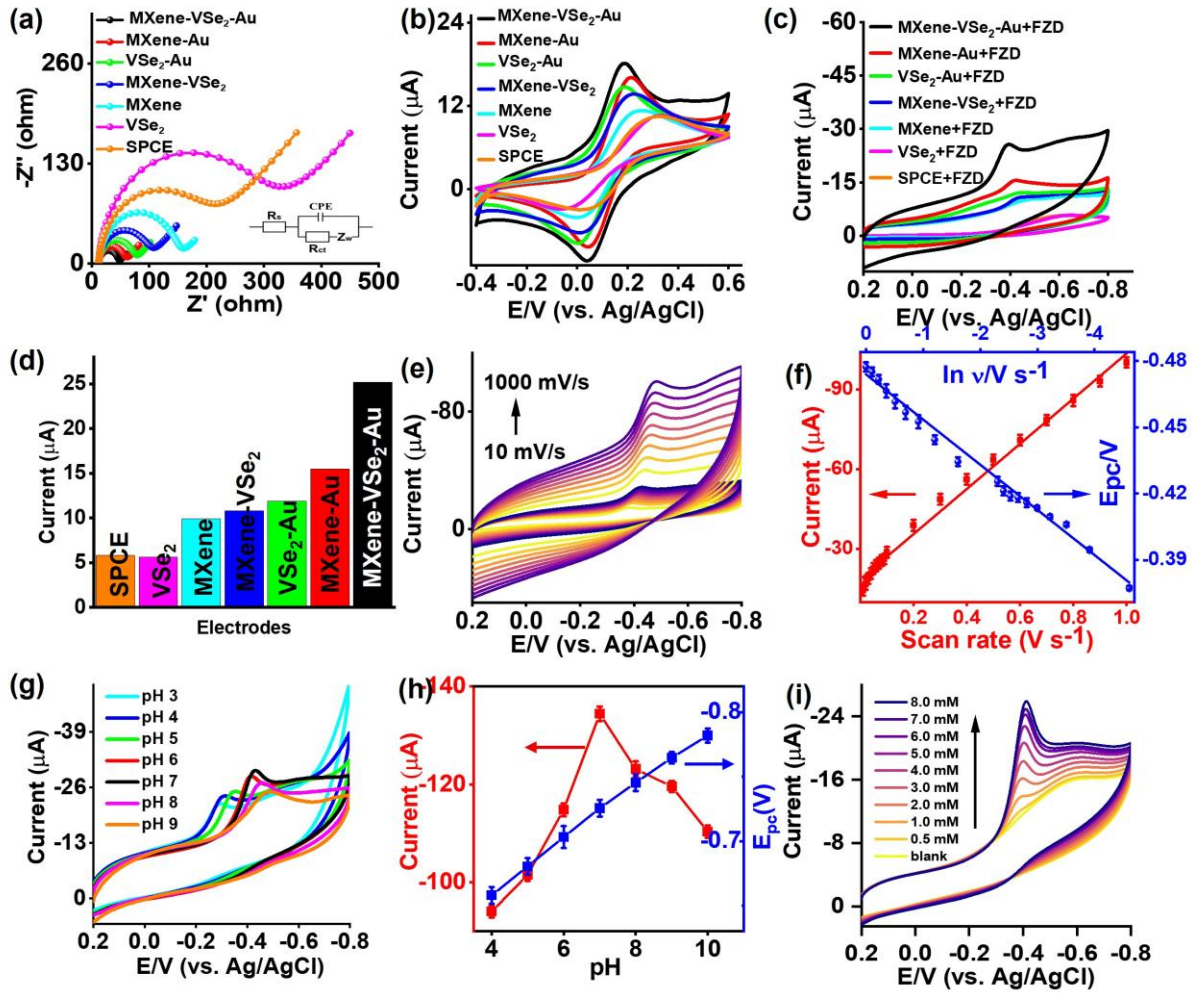

Figure 4: (a-b) EIS plots and CV response of different sensors in 5 mM $[Fe(CN)_6]^{3-/4-}$ and 0.1 KCl (inset: Randles equivalent circuit). (c-d) CV profiles of the different electrodes in the presence or absence of

FZD in N_2 saturated 0.05 M PBS (pH 7) solution. (e-f) CV profiles of Au-VSe_2-MXene sensor at different sweep rates (10-1000 mV/s) in 0.05 M PBS containing 200 μM FZD. Plot of cathodic signal intensity vs. sweep rate for Au-VSe_2-MXene sensor. (g) CV profile of Au-VSe_2-MXene sensor in 0.05 M PBS solution containing FZD at different concentrations. (h-i) presents the CV profiles of Au-VSe_2-MXene sensor in 0.05 M PBS at varying pH values in the presence of FZD, recorded at a sweep rate of 50 mV/s, along with plots of cathodic peak current and peak potential as functions of pH.

The volume of Au-VSe_2-MXene sensing material suspension deposited on the electrode critically governs the density of accessible catalytic sites. Its effect was evaluated by drop-casting 1.0-6.0 μL of suspension and recording the electrochemical response toward 500 μM FZD in 0.05 M PBS (pH 7.0) via CV (Figure SI 3). The cathodic peak current increased linearly between 1.0 and 3.0 μL, reflecting expansion of the electroactive surface area. At volumes ≥4.0 μL, signal attenuation occurred, attributed to formation of a thicker film that impeded electron transfer and analyte diffusion. Thus, 4.0 μL was selected as optimal. Preconcentration further improved analytical performance. SWV studies in PBS (pH 7.0, 100 nM FZD) showed that the cathodic response increased with accumulation time up to 150 s, indicating surface adsorption, then plateaued due to saturation (Figure SI 4). An accumulation time of 60 s balanced sensitivity and stability. Varying accumulation potential (+0.2 to -0.4 V) revealed a maximum response at -0.4 V, established as optimal for FZD detection.

Electrolyte pH strongly influenced FZD reduction. CV measurements of 200 μM FZD across pH 3-9 demonstrated increasing cathodic currents from pH 3 to 7, followed by decline at higher pH, identifying pH 7 as optimal (Figure 4g-h). The cathodic potential shifted positively with pH, indicating proton

involvement and easier FZD deprotonation during reduction. A linear E_{pc}-pH relationship, E_{pc} (V) = -0.0208 pH - 0.577 (R^2 = 0.9976), yielded a slope significantly below the Nernstian 59 mV pH^{-1}. Using the Nernst equation, the m/n ratio was 0.35 (1 H^+ per 2.9 e^-), indicating non-stoichiometric proton-electron participation in FZD electrocatalysis. Maximum cathodic current at pH 7 was used for subsequent sensing studies, confirming the Au-VSe_2-MXene sensor as a highly efficient platform for sensitive FZD detection.

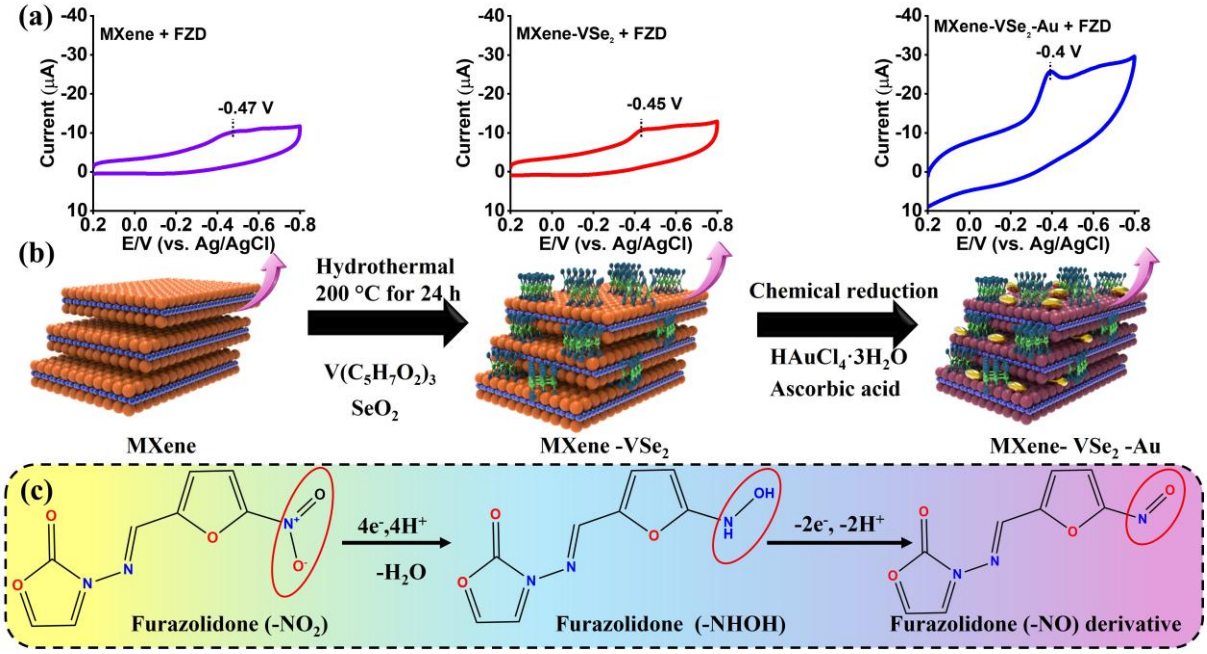

Scheme 1: (a) CV of Au-VSe_2-MXene sensor in 0.05 M PBS containing 500 µM FZD (pH 7.0) at a scan rate of 30 mV s^{-1}; (b) Conceptual schematic of the Au-VSe_2-MXene sensor nanosheet configuration; (c) Proposed electrocatalytic reduction mechanism of FZD on the Au-VSe_2-MXene sensor.

3.4 Electrocatalytic FZD quantification

The electrochemical performance of the Au-VSe_2-MXene sensor toward FZD reduction was assessed via CV, LSV, and chronoamperometry. CV analyzes confirmed pronounced electrocatalytic activity, showing a linear cathodic peak increase from 0.5 to 8 mM (Figure 4i), with slight positive peak shifts at higher concentrations attributed to enhanced FZD adsorption at the electrode-electrolyte interface. The Au-VSe_2-MXene sensor exhibited high catalytic efficiency at low overpotentials, minimizing fouling and interference. Au incorporation into the VSe_2-MXene matrix improved electron transport, markedly enhancing FZD detection at reduced potentials. LSV data revealed progressive cathodic signal enhancement with increasing FZD, defining a working range of 1-500 μM in N_2-saturated PBS (pH 7.0) (Figure SI5). The composite's high surface area accelerated electron-transfer kinetics and electrocatalytic efficiency.

Chronoamperometry (i-t), distinguished by high sensitivity and temporal resolution, was employed to assess the electrocatalytic activity and FZD detection capability of the Au-VSe_2-MXene sensor (Figure 5a-b). The chronoamperometric response was recorded following successive dropwise FZD additions at applied potentials of -0.38 to -0.42 V (vs. Ag/AgCl) in N_2-saturated 0.05 M PBS (pH 7.0). Under controlled hydrodynamic conditions (-0.40 V, 1200 rpm), the transient current attained 95% of its steady-state value within 3 s, reflecting rapid electron-transfer kinetics and pronounced electrocatalytic activity at the Au-VSe_2-MXene sensor interface. The calibration curve exhibited a linear cathodic current response to FZD over a broad range from 6.0 to 225 nM, with distinct current steps transitioning from linearity at low concentrations to saturation at higher levels. The sensor achieved a steady-state response within <3 s, reflecting rapid electrocatalytic kinetics and the formation of a thin diffusion layer. At elevated FZD levels, signal attenuation accompanied by increased noise and reduced faradaic current

indicated a shift to a diffusion-limited electron-transfer regime. Linear regression was expressed as I (μA) = 0.04216[FZD] (nM) + 1.920 (R^2 = 0.9383). Based on the calibration slope (S) and blank standard deviation (σ = 0.003 μA, n = 5), the limit of detection and quantification were 0.21 nM and 0.71 nM, respectively. Normalized sensitivity was 0.597 μA nM^{-1} cm^{-2}. These results demonstrate that the Au-VSe_2-MXene sensor combines high sensitivity, rapid response, and a wide dynamic range, making it a robust platform for trace-level FZD detection. The Au-VSe_2-MXene sensor exhibited superior analytical performance, combining a low detection limit with a broad linear dynamic range relative to reported FZD sensors (Table S2). The VSe_2-MXene scaffold provides high surface area to suppress Au nanoparticle aggregation, while its conductive network minimizes electron-transfer resistance. This synergistic integration enhances nanocomposite conductivity, yielding a sensor with high sensitivity, low detection limits, and robust applicability for trace-level FZD analysis in real samples.

3.5 Smartphone integrated FZD detection using Au-VSe_2-MXene sensor

The practical feasibility of the Au-VSe_2-MXene-modified RDE was evaluated for FZD detection in real samples, including hospital wastewater, pond, river, and lake water, using the standard addition method. Water samples collected from Inha University, Incheon, South Korea, were diluted 1:1 with 0.05 M PBS (pH 7.0). Amperometric measurements were performed at -0.4 V (vs. Ag|AgCl) with successive injections of known FZD concentrations (Figure 5c-f). The cathodic response increased systematically with each addition of FZD-spiked sample, and quantification was achieved via calibration plots correlating current with concentration (Figure SI 6-7). The sensor exhibited excellent recoveries: 95.3-104.6% (hospital), 93.1-108.2% (pond), 98.2-105.2% (river), and 100.3-103.3% (lake), with all RSDs

below 5% (Table S3-4). Strong agreement with UV-Vis analyses (Figure SI 8) further validated its applicability for rapid, selective detection in complex matrices (Figure 5c). This demonstration confirms the Au-VSe_2-MXene sensor's capability for real-time, on-site FZD monitoring in environmental samples.

Anti-interference and specificity studies confirmed robust performance for trace-level environmental monitoring. Amperometric measurements in 30 nM FZD (N_2-saturated PBS, pH 7.0) in the presence of 200 nM potentially interfering metal ions (Cd^{2+}, K^+, Pb^{2+}, NO_3^- and SO_4^{2-}), biological compounds (dopamine, uric acid, ascorbic acid), organic species, nitro compounds, and structurally related antibiotics (50 nM) showed minimal changes in cathodic currents (<5%, Figure SI 9). This exceptional tolerance is attributed to the synergistic design of the hybrid material: the VSe_2-MXene matrix promotes FZD adsorption via π-π stacking and hydrogen bonding interactions, while AuNPs catalyze nitro group reduction. Hydrogen bonding between surface hydroxyls and FZD carbonyl groups likely facilitates preconcentration and molecular orientation. Even at elevated interferent concentrations, FZD detection remained reliable. Collectively, these results demonstrate that the Au-VSe_2-MXene sensor is a highly sensitive, selective, and robust platform suitable for environmental, agricultural, and medical FZD monitoring, offering rapid, on-site, real-time sensing with minimal sample preparation and broad applicability across diverse matrices.

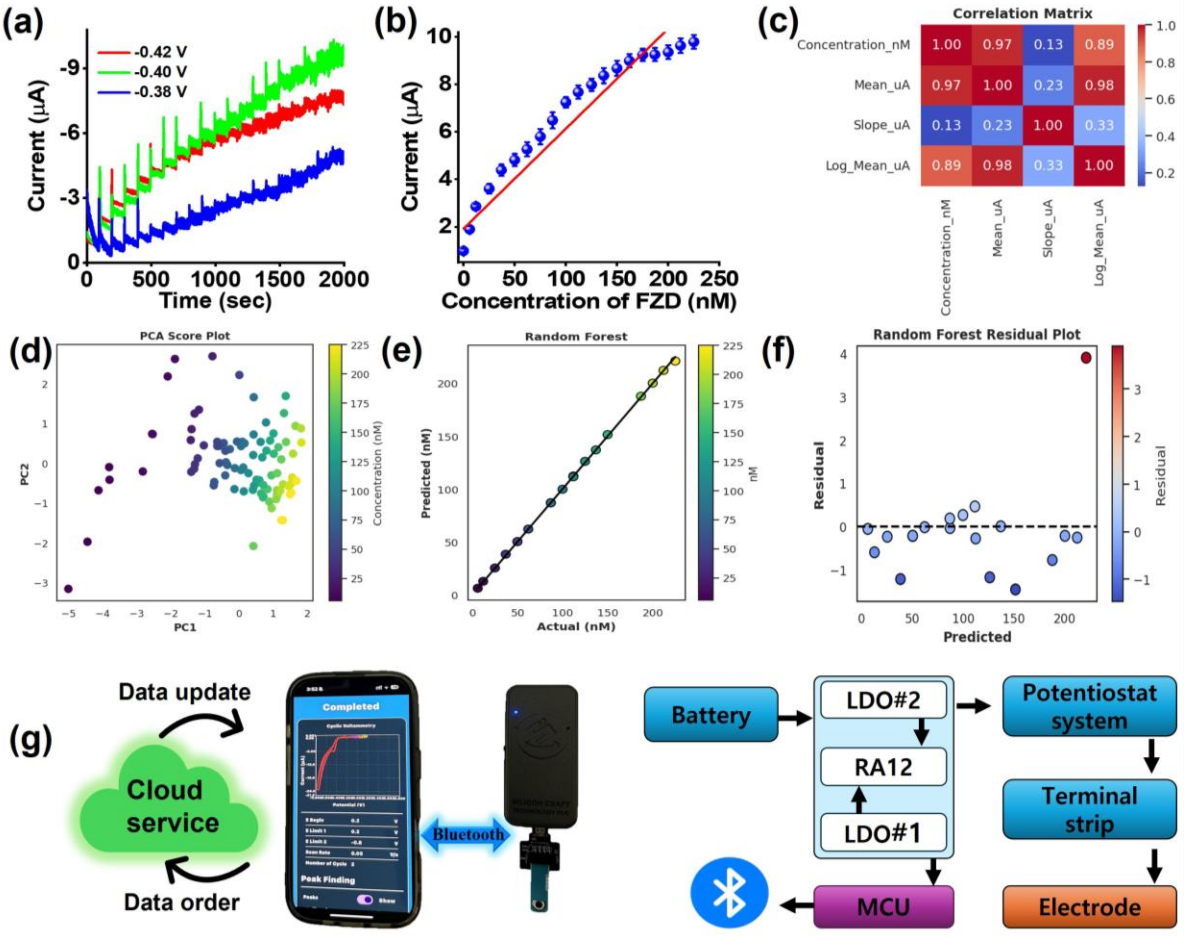

Figure 5: (a-b) Chronoamperometric (i-t) responses of Au-VSe_2-MXene sensor to successive FZD additions (6-225 nM) in N_2-saturated 0.05 M PBS (pH 7.0); inset: calibration curve of current (μA) versus FZD concentration (nM). (c) Correlation matrix illustrates the relationship between electrochemical features (Mean current, Slope, and Logarithmic mean current) and FZD concentration. (d) PCA score plot showing concentration-dependent distribution of samples in reduced dimensional space (e) Predicted versus actual concentration plots obtained using Random Forest. (f) Residual plots for Random Forest model showing prediction error distribution. (g) Schematic of a

portable electrochemical sensor integrated with MCU, potentiostat, and wireless data transmission.

Reusability, reproducibility, repeatability, and long-term stability are key metrics for assessing the practical viability of the Au-VSe_2-MXene sensor. Reproducibility was evaluated via SWV using ten independently prepared electrodes in 20 nM FZD (N_2-saturated PBS, pH 7.0). The cathodic currents exhibited minor variations, likely due to handling, with an RSD of 4.6% (Figure SI 10). Repeatability was assessed with a single electrode performing ten consecutive measurements of 20 nM FZD, yielding a slight decrease in current response and an RSD of 3.6%, attributable to partial surface saturation (Figure SI 11). Sensor regenerability was tested over eight analytical cycles, with electrode regeneration by immersion in deionized water for 3 min followed by 10 min air-drying between measurements. After eight cycles, 89.8% of the initial current was retained (RSD 4.8%, Figure SI 12). Long-term stability was investigated using a stored electrode (4 °C) with measurements of 20 nM FZD over 30 days, showing 92.6% current retention (RSD 4.04%) with minimal biofouling effects (Figure SI 13). XRD analysis post-stability testing revealed no structural changes in the electrode (Figure SI 14). Collectively, these results demonstrate that the Au-VSe_2-MXene sensor exhibits excellent reproducibility, repeatability, reusability, and stability, supporting its suitability for reliable environmental FZD monitoring.

3.6 Machine learning-assisted FZD detection with IoT deployment

Although the Au-VSe_2-MXene sensor exhibits a strong linear response toward FZD ($R^2 = 0.9383$), conventional calibration remains vulnerable to signal fluctuations caused by experimental variability, electrode heterogeneity, and mass transport effects, particularly at low and high concentration ranges [39]. To address these limitations and enable reliable real-time analysis,

machine learning (ML) was employed to establish a robust relationship between electrochemical features and analyte concentration. Unlike single-parameter linear fitting, ML models capture subtle nonlinear dependencies by integrating multiple signal descriptors. Correlation analysis shows that mean current is the dominant predictor (R = 0.97), while its logarithmic transformation (R = 0.89) captures slight nonlinearity. The slope exhibits weak individual correlation (R = 0.13) but contributes complementary information related to transient behavior. Principal component analysis (PCA) confirms feature suitability, with PC1 (71%) and PC2 (29%) accounting for nearly all variance and demonstrating clear concentration-dependent separation. Multiple regression models were compared to identify optimal performance (Figure 5c-f). All models showed strong agreement between predicted and actual values, confirming effective feature representation. Random Forest achieved the highest accuracy (R^2 = 0.9997, RMSE = 1.07 nM, MAE = 0.61 nM), followed by Linear Regression (R^2 = 0.9960), while KNN (R^2 = 0.9262) and MLP (R^2 = 0.9529) showed lower performance with higher errors [40]. All ML models significantly outperformed conventional linear calibration (R^2 = 0.9383), with improved accuracy arising from the inclusion of multiple descriptors capturing minor nonlinearities (Table S5). The strong performance of Linear Regression indicates predominantly linear behavior, while the superior accuracy of Random Forest reflects its ability to model subtle nonlinear effects and reduce noise sensitivity [41]. Lower performance of KNN and MLP is attributed to sensitivity to data distribution and limited dataset size, affecting generalization [42]. Five-fold cross-validation and hyperparameter optimization ensured reliable evaluation (Table S6). Training and validation curves indicate stable generalization for Linear Regression and Random Forest, while KNN and MLP show variability [43]. Residual

analysis further supports these findings, with Random Forest exhibiting minimal deviation. Feature importance confirms that mean current and its logarithmic form dominate prediction. Random Forest was selected for deployment due to its robustness and generalization capability (Figure SI 15-19).

The sensing patch integrates an NFC antenna, NT3H2111 NFC chip (NXP), MSP430FR2632 microcontroller, TLV2401-based analog front-end, and an electrode array. The NFC chip harvests energy and regulates the supply (~2.76 V) to power the MCU and signal-processing circuitry. Electrochemical signals from the three-electrode system are conditioned via biasing, buffering, and low-pass filtering, and digitized using integrated ADCs. Measurements employ a portable potentiostat with screen-printed carbon and Ag/AgCl as counter and reference electrodes (Figure 5g). The system incorporates an SIC824B sensing module with Bluetooth® 5.2 and operates on a 320 mAh rechargeable battery. A USB-enabled potentiostat coupled with a smartphone enables real-time voltammetric analysis (<1 min) using ~30 μL samples. Data are transmitted to a cloud platform hosting a trained FZD model via Streamlit Cloud and GitHub, enabling.xlsx upload, signal visualization, and remote qualitative detection within an IoT-enabled framework. Overall, the multivariate ML approach significantly enhances accuracy, robustness, and reliability compared to conventional calibration.

4 Conclusion

In summary, AuNPs were integrated into a VSe_2-decorated MXene nanoarchitecture through a one-step hydrothermal synthesis, followed by a subsequent chemical reduction process. The

resulting Au-VSe_2-MXene sensor enabled rapid and precise sensing of FZD in environmentally polluted samples. Electrochemical impedance and voltammetric analyses indicated low charge-transfer resistance (45 Ω) and rapid heterogeneous electron-transfer kinetics (up to 1.68×10^{-2} cm s^{-1}) at the Au-VSe_2-MXene sensor interface. The electrode delivered exceptionally high cathodic currents for trace-level FZD reduction at -0.40 V (vs. Ag/AgCl). Amperometric measurements demonstrated that the optimized sensor provided a wide linear dynamic range (6-255 nM), high sensitivity (0.597 μA nM^{-1} cm^{-2}), and an ultralow detection limit (0.21 nM). The platform showed strong analytical robustness, with repeatability of 3.6%, reproducibility of 4.6% across ten measurements, 89.8% retention of the initial response after eight regeneration cycles, and 92.6% activity retention after 30 days. During real-time measurements, the electrode showed high tolerance to interfering species, emphasizing its potential for direct on-site FZD sensing. Recovery studies further exhibited excellent accuracy, with values ranging from 93.1% to 108.2% and relative standard deviations below 5.0% in hospital wastewater, pond, river water, and lake water. Cathodic currents from amperometric i-t responses were analyzed using an optimized tree-based machine learning models for accurate FZD concentration predicition, while IoT support allowed remote sensing and straightforward data access. Future developments involving larger datasets and real sample conditions are expected to further improve model robustness and enable the growth of fully portable intelligence sensing systems that can perform on-site decision-making and adaptive analysis in intricate environmental contexts.

Acknowledgments

This work was supported by the 2025 Dongguk University,South korea HCR Track Faculty Support Program.

Competing interests

The authors declare no competing interests.

Supplementary Information

Below is the link to the electronic supplementary material.

References

1. Mady AH, Baynosa ML, Saad M, Dhakal G, Tuma D, Kim WK, et al. Morphology-engineered hollow $NiTiO_3$/C–Ag/Ag_3PO_4 S-scheme heterojunction photocatalyst: mechanistic insights into sunlight-driven tetracycline degradation. Advanced Composites and Hybrid Materials. 2026;9(2):108. doi: 10.1007/s42114-025-01600-x.
2. Karikalan N, Lee TY. Laser-driven molecular hybridization of $Sm(OH)_3$:Se nanocomposites with tailored electronic states for antibiotics sensing. Advanced Composites and Hybrid Materials. 2026;9(2):130. doi: 10.1007/s42114-026-01676-z.
3. Yang L, Feng A, Zhang H, Wang H, Wei X, Wang Z, et al. Laser-induced graphene nanocomposites with molecularly imprinted polymers and Prussian blue for electrochemical sensing of vitamin B6 and glucose. Composites Part B: Engineering. 2025;304:112843. doi: https://doi.org/10.1016/j.compositesb.2025.112843.
4. Zhang Q, Cheng Y, Yin X, Wang C, Wu Q, Ma J, et al. CuS hollow nanocages with rough surface to enhanced photothermal property for ultra-sensitive detection of furazolidone metabolites. Chemical Engineering Journal. 2024;498:155153. doi: https://doi.org/10.1016/j.cej.2024.155153.
5. Liu R, Wu B, Xu C, Zhang C, Han M, Zhao M, et al. Ultrasonically assisted synthesis of Co-Ni

bimetallic oxides for simultaneous detection of furazolidone and metronidazole. Ultrasonics Sonochemistry. 2025;120:107433. doi: https://doi.org/10.1016/j.ultsonch.2025.107433.
6. Nguyen TA, Nagari A, Ong VH, Van Manh T, Tufa LT, Lee J, et al. Visible Light-Assisted Detection of Furazolidone Using a Ag@Fe_3O_4 Nanoparticle-Based Electrochemical Sensor. Langmuir. 2025;41(27):17543-54. doi: 10.1021/acs.langmuir.5c00947.
7. Sonwal S, Ranjith KS, Han S, Han Y-K, Oh M-H, Huh YS. Live-tracking of beef freshness by sub-ppb level ammonia detection using WS_2/rGO nanoflakes incorporating edge site-enriched acidic sulfur. Journal of Materials Chemistry A. 2024;12(18):11004-19. doi: 10.1039/D3TA07831K.
8. Kokulnathan T, Almutairi G, Chen S-M, Chen T-W, Ahmed F, Arshi N, et al. Construction of Lanthanum Vanadate/Functionalized Boron Nitride Nanocomposite: The Electrochemical Sensor for Monitoring of Furazolidone. ACS Sustainable Chemistry & Engineering. 2021;9(7):2784-94. doi: 10.1021/acssuschemeng.0c08340.
9. Sonwal S, Alhammadi M, Han S, Kumar GS, Han Y-K, Oh M-H, et al. Advancements in pretreatment-free portable sensing approaches for antibiotics detection in non-invasive livestock samples: Assessment and requirement of positive list system regulations. Trends in Environmental Analytical Chemistry. 2025;47:e00272. doi: https://doi.org/10.1016/j.teac.2025.e00272.
10. Selvam Sp, Vinothini S, Chen S-M, Chiu TW. Electrochemical Sensor Based on Lead Molybdate–Carbon Nanocomposite for the Detection of Furazolidone. ACS Applied Nano Materials. 2025;8(49):23701-14. doi: 10.1021/acsanm.5c04572.
11. Kong D, Liang B, Yun H, Ma J, Li Z, Wang A, et al. Electrochemical degradation of nitrofurans furazolidone by cathode: Characterization, pathway and antibacterial activity analysis. Chemical Engineering Journal. 2015;262:1244-51. doi: https://doi.org/10.1016/j.cej.2014.10.094.
12. Veerakumar P, Sangili A, Chen S-M, Pandikumar A, Lin K-C. Fabrication of Platinum–Rhenium Nanoparticle-Decorated Porous Carbons: Voltammetric Sensing of Furazolidone. ACS Sustainable Chemistry & Engineering. 2020;8(9):3591-605. doi: 10.1021/acssuschemeng.9b06058.
13. Nehru R, Chen C-W, Dong C-D. Recent advances in electrochemical detection of furazolidone:

A review. Microchemical Journal. 2024;197:109901. doi: https://doi.org/10.1016/j.microc.2024.109901.
14. Yadav A, Patel C, Kanwar JR, Sriram S, Mukherjee S. Miniaturized IoT-enabled MoS_2-based electrochemical sensor for real-time adenine monitoring. Journal of Electroanalytical Chemistry. 2025;999:119564. doi: https://doi.org/10.1016/j.jelechem.2025.119564.
15. Yan D, Zhu B, Wang J, Wu M, Xie F, Qi P, et al. Wireless portable intelligent nanosensor for pretreatment-free, anti-interference, and real-time on-site detection of furazolidone in fish products. LWT. 2025;230:118275. doi: https://doi.org/10.1016/j.lwt.2025.118275.
16. Sarathkumar E, Jayasree RS. Machine learning-integrated lateral flow assays: Unlocking the future of intelligent point-of-care sensing. TrAC Trends in Analytical Chemistry. 2025;193:118478. doi: https://doi.org/10.1016/j.trac.2025.118478.
17. Lahari SA, Kumawat N, Amreen K, Ponnalagu RN, Goel S. IoT integrated and deep learning assisted electrochemical sensor for multiplexed heavy metal sensing in water samples. npj Clean Water. 2025;8(1):10. doi: 10.1038/s41545-025-00441-x.
18. Hilal M, Fayaz H, Ali Y, Park S, Petrů J, Bashir MN, et al. Quantum-engineered $Ti_3C_2T_x$-QD@V_2CT_x hybrid composite with Ti–O–V interfacial bonding for extreme-humidity H_2S sensing. Advanced Composites and Hybrid Materials. 2026;9(2):106. doi: 10.1007/s42114-026-01646-5.
19. Guo R, Li S, Duan R, Sun Y, Li J, Wu Y, et al. Defect-interface engineering optimizes polymetallic sulfides-based absorbers toward high-efficiency low-/middle-frequency electromagnetic wave absorption. Advanced Composites and Hybrid Materials. 2025;8(6):455. doi: 10.1007/s42114-025-01541-5.
20. Ye J, Ali H, Sawwan H, Alsaikhan K, Jery AE, Alenad AM, et al. Efficient visible-light-responsive CN/In_2O_3/MoO_3 heterojunctions for sustainable H_2 generation and environmental remediation. Advanced Composites and Hybrid Materials. 2026;9(2):113. doi: 10.1007/s42114-026-01671-4.
21. Kwak IH, Kim JY, Zewdie GM, Yang J, Lee K-S, Yoo SJ, et al. Electrocatalytic Activation in $ReSe_2$-VSe_2 Alloy Nanosheets to Boost Water-Splitting Hydrogen Evolution Reaction. Advanced Materials. 2024;36(15):2310769. doi: https://doi.org/10.1002/adma.202310769.

22. Vilian E, Ahn J, Mohammadi A, Hormozi Jangi SR, Mohammadzadeh L, Choo J, et al. An AI-assisted smartphone platform for H_2O_2 and glutathione detection using a dual-functional Pd-ReS_2-MXene nanoprobes. Biosensors and Bioelectronics. 2026;295:118287. doi: https://doi.org/10.1016/j.bios.2025.118287.
23. Ahn J, Mohammadi A, Kumar K, Pachin MO, Tamang S, Xu Y, et al. Pt–VS_2–MXene nanozyme for on-site pesticide and H_2O_2 sensing: Bridging computational insights and experiment. Sensors and Actuators B: Chemical. 2026;446:138717. doi: https://doi.org/10.1016/j.snb.2025.138717.
24. Xu G, Fei B, Xu J, Hu Z, Wang C, Han Y, et al. Coupling of Defective VSe_{2-x} with Graphene via V─C Bonds for High-Rate and Long-Life Sodium-Ion Storage. Small. 2025;21(48):e09002. doi: https://doi.org/10.1002/smll.202509002.
25. Ezhil Vilian AT, Tiwari JN, Alhammadi M, Bhaskaran G, Hwang S-K, Kim S, et al. Palladium nanoparticles anchored MoS_2-MXene composite modified electrode for rapid sensing of toxic bisphenol A in aqueous media. Chemical Engineering Journal. 2023;469:144017. doi: https://doi.org/10.1016/j.cej.2023.144017.
26. Tiwari JN, Kumar K, Safarkhani M, Umer M, Vilian ATE, Beloqui A, et al. Materials Containing Single-, Di-, Tri-, and Multi-Metal Atoms Bonded to C, N, S, P, B, and O Species as Advanced Catalysts for Energy, Sensor, and Biomedical Applications. Advanced Science. 2024;11(33):2403197. doi: https://doi.org/10.1002/advs.202403197.
27. Jeong S, Park S-H, Lee S, Cho H, Lee K-y, Ju BK, et al. Electrochemical biosensor based on gold nanoparticles/laser induced graphene for diagnosis of Parkinson's disease by detecting phosphorylated α-synuclein in human blood. Chemical Engineering Journal. 2025;509:161329. doi: https://doi.org/10.1016/j.cej.2025.161329.
28. Mani A, Anirudhan TS. Electrochemical sensing of cortisol by gold nanoparticle incorporated carboxylated graphene oxide based molecularly imprinted polymer. Chemical Engineering Journal. 2024;493:152654. doi: https://doi.org/10.1016/j.cej.2024.152654.
29. Guan M, Huang Z, Bao Z, Ou Y, Zou S, Liu G. Gold nanoparticles incorporated liquid metal for wearable sensors and wound healing. Chemical Engineering Journal. 2025;508:161120. doi:

https://doi.org/10.1016/j.cej.2025.161120.
30. Tu W, Sun M, Lu T, Chen Y, Zhou Y, Zhang C, et al. Wearable electrochemical aptasensor based on MXene@gold nanoparticles for non-invasive sweat cortisol detection. Biosensors and Bioelectronics. 2025;287:117736. doi: https://doi.org/10.1016/j.bios.2025.117736.
31. Haotian R, Zhu Z, Zhang H, Lv T, Tang S, Zhang J, et al. Engineering conductive covalent-organic frameworks enable highly sensitive and anti-interference molecularly imprinted electrochemical biosensor. Biosensors and Bioelectronics. 2025;273:117195. doi: https://doi.org/10.1016/j.bios.2025.117195.
32. Nezafat Z, Jafari G, Javanshir S, Peymanfar R. MXene-based metal oxide/metal composites for microwave absorption and shielding: recent advances and future perspectives. Advanced Composites and Hybrid Materials. 2025;8(6):447. doi: 10.1007/s42114-025-01535-3.
33. Tiwari JN, Umer M, Bhaskaran G, Umer S, Lee G, Kim MG, et al. Atomic layers of ruthenium oxide coupled with $Mo_2TiC_2T_x$ MXene for exceptionally high catalytic activity toward water oxidation. Applied Catalysis B: Environmental. 2023;339:123139. doi: https://doi.org/10.1016/j.apcatb.2023.123139.
34. Purbayanto MAK, Presser V, Skarżyński K, Słoma M, Naguib M, Jastrzębska AM. MXenes: Multifunctional Materials for the Smart Cities of Tomorrow. Advanced Functional Materials. 2025;35(10):2409953. doi: https://doi.org/10.1002/adfm.202409953.
35. Rahman M, Al Mamun MS. Future prospects of MXenes: synthesis, functionalization, properties, and application in field effect transistors. Nanoscale Advances. 2024;6(2):367-85. doi: 10.1039/D3NA00874F.
36. Randviir EP. A cross examination of electron transfer rate constants for carbon screen-printed electrodes using Electrochemical Impedance Spectroscopy and cyclic voltammetry. Electrochimica Acta. 2018;286:179-86. doi: https://doi.org/10.1016/j.electacta.2018.08.021.
37. Laviron E. Adsorption, autoinhibition and autocatalysis in polarography and in linear potential sweep voltammetry. Journal of Electroanalytical Chemistry and Interfacial Electrochemistry. 1974;52(3):355-93. doi: https://doi.org/10.1016/S0022-0728(74)80448-1.
38. Velasco JG. Determination of standard rate constants for electrochemical irreversible processes

from linear sweep voltammograms. Electroanalysis. 1997;9(11):880-2. doi: https://doi.org/10.1002/elan.1140091116.
39. Bocan A, Siavash Moakhar R, del Real Mata C, Petkun M, De Iure-Grimmel T, Yedire SG, et al. Machine-Learning-Aided Advanced Electrochemical Biosensors. Advanced Materials. 2025;37(33):2417520. doi: https://doi.org/10.1002/adma.202417520.
40. Sarathkumar E, Menon RN, Jayasree RS. Ultrasensitive SERS-LFA for the detection of neurofilament light chain and machine learning-assisted Alzheimer's disease classification. Nanoscale. 2025;17(44):25616-30. doi: 10.1039/D5NR03475B.
41. Kadian S, Kumari P, Shukla S, Narayan R. Recent advancements in machine learning enabled portable and wearable biosensors. Talanta Open. 2023;8:100267. doi: https://doi.org/10.1016/j.talo.2023.100267.
42. Ying H, Song M, Tang Y, Xiao S, Xiao Z. Enhancing deep neural network training efficiency and performance through linear prediction. Scientific Reports. 2024;14(1):15197. doi: 10.1038/s41598-024-65691-0.
43. Li A, Yang H, Yu W, Liu T, Luo B, Zhao C. Application of machine learning to improve the accuracy of electrochemical sensors: A review. TrAC Trends in Analytical Chemistry. 2025;193:118469. doi: https://doi.org/10.1016/j.trac.2025.118469.

Supplementary Files

This is a list of supplementary files associated with this preprint. Click to download.

- SupplementaryMaterial.docx